Robust Design of a Decoupled Vibratory Microgyroscope Considering Over-Etching as a Fabrication Tolerance Factor[*]

Sung Kyu HA[**], Hee-Moon JEONG[***] and JunO KIM[***]

A robust optimal design of a bulk-micromachined, decoupled vibratory microgyroscope was carried out to determine geometric dimensions such that the gyroscopic performance is least affected by a fabrication tolerance. Electro-mechanical vibration analysis considering the sensing electrodes and the electronic signal processing were performed to obtain the frequency responses that influence the gyroscopic performance. A statistically distributed lateral over-etching (*LOE*) developed in the fabrication process was selected as a fabrication tolerance factor. The dimensions of the driving and sensing spring are selected as design variables which are the sum of deterministic mask dimensions and the *LOE*. To minimize the influence of *LOE* on the decoupled vibratory microgyroscope performance, the multi-objective function was formulated so as to minimize the sensitivities of the frequency difference with respect to the *LOE*. As a result, the standard deviation of the frequency difference and the driving natural frequency are reduced to 78% and 8%, respectively, through the Monte Carlos Simulation (MCS).

Key Words: MEMS Fabrication Tolerance, Over-Etching, Decoupled Vibratory Microgyroscope, Robust Design, Optimization

1. Introduction

A number of silicon micromachined vibratory microgyroscopes have been widely developed due to the merits of low cost, small size and compatibility with IC process[(1),(2)]. The basic principle employed in the vibratory microgyroscope is the Coriolis acceleration effect[(1),(3)]. Most vibratory microgyroscopes have comb drives for driving and capacitive electrodes for sensing motion because the electrodes can be easily embodied by micro-electro-mechanical system (MEMS) fabrication[(4)–(6)]. To improve its performance, the vibratory microgyroscope was designed as a decoupled system between driving and sensing structures[(5)–(8)] and the driving structure vibrates at its natural frequency[(1),(4),(9)]. The decoupled system improved the signal-to-noise ratio by reducing the quadrature signal error[(5),(7)]. It also gave the designer more freedom in designing the driving and sensing frequencies independently. The scale factor (or sensitivity) of the gyroscope is proportional to the driving displacement[(5)]. When the driving structure vibrates at its natural frequency, the displacement is magnified in proportion to mechanical quality factor (Q factor).

The MEMS fabrication process considerably influences the yield of the gyroscope, and it should be considered in the design process. The scale factor of the vibratory microgyroscope depends on the frequency difference between the driving and the sensing structures[(9)]. The variation in the structural dimension due to the fabrication error gives rise to the variation in the frequency difference and eventually reduces the gyroscope yield satisfying the performance specifications. In the fabrication process minimization of the fabrication error is essential in increasing the yield[(10),(11)] but in the design stage a robust design to minimize the fabrication tolerance must be considered in order to increase the yield and to reduce production cost. Hwang et al.[(12)] have performed an axiomatic design and then a robust design using Taguchi concept[(13),(14)] for the robust performance regardless of the tolerance. However, since it needs to calculate the standard deviation, it requires excessive calculation time. Han et al.[(15)] obtained the robustness of the objective func-

tion by minimizing the gradient of the response to uncertain variables in the coupled vibratory microgyroscope. However, the proposed objective formulation, which minimizes the maximum sensitivity of the frequency difference, is not adequate for the decoupled vibratory microgyroscope.

This paper presents a robust optimal design for the decoupled vibratory microgyroscope considering fabrication influence. An over-etching, which has a statistical distribution and affects all structural dimensions at the same time, was modeled as a fabrication tolerance factor. Also the newly defined design variables having two components were presented for considering the fabrication tolerances. To minimize the influence of the fabrication tolerance factor on the decoupled vibratory microgyroscope performance, the robust optimal design was performed. The dimensions of the driving and sensing spring were adopted as design variables, and the multi-objective function was formulated so as to minimize the sensitivity of the frequency difference and the sensitivity of the frequency itself. The results of the robust optimal design were certified using the Monte Carlos Simulation (MCS).

2. Modeling of a Decoupled Microgyroscope

2.1 Concept design of the decoupled microgyroscope

A decoupled, lateral vibratory microgyroscope considered in the present research is illustrated in Fig. 1. It consists of a driving structure and a sensing structure. The driving structure is driven by the comb drive in the x-direction. The sensing structure, connected to the driving structure through the sensing spring, oscillates in the y-direction due to the Coriolis acceleration relatively to the driving motion. Two sets of comb sensors are implemented in this gyroscope: the driving sensor comb for sensing the driving motion and the sensing electrodes for sensing the sensing motion. Due to the symmetry of the sensing electrodes with respect to the y-axis, the sensing
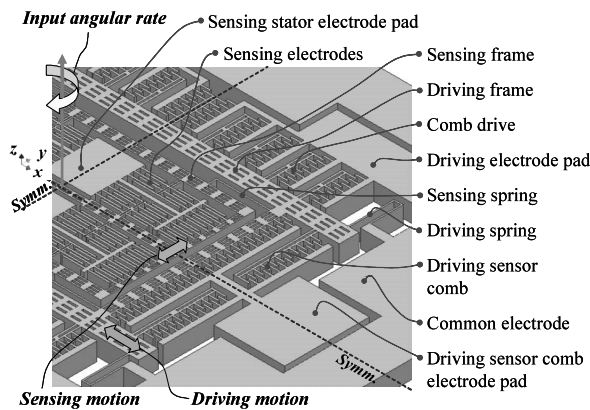
capacitance in the sensing structure does not change by the driving motion.

2.2 Dynamic modeling of the electro-mechanical system

The schematic diagram of the decoupled microgyroscope is shown in Fig. 2, and its dynamic equations can be written as follows:

$$\begin{bmatrix} m_a & 0 \\ 0 & m_s \end{bmatrix} \ddot{u} + \begin{bmatrix} c_a & 0 \\ 0 & c_s \end{bmatrix} \dot{u} + \begin{bmatrix} k_a & 0 \\ 0 & k_s \end{bmatrix} u = F \qquad (1)$$

where the subscripts a and s represent the driving and the sensing components. The symbols m, c, k, u and F represent the mass, the damping coefficient, the spring constant (see Appendix A), the two dimensional displacement and force vectors, respectively.

The movable structure is oscillated in driving direction by the driving force that consists of DC voltage V_b and AC voltage $v_a(t)$ with the magnitude V_a and the driving frequency ω. When the input angular velocity with the amplitude Ω_0 and the frequency ω^R is applied on z-axis of the gyroscope, the Coriolis force is generated and then the sensing displacement occurs by the force. The force vector, which consists of driving force $F_a(t)$ and Coriolis force $F_s(t)$, and the displacement vector are calculated and expressed as follows:

$$F(t) = \left\{ \begin{array}{c} F_a^0 \mathrm{Im}[e^{j\omega t}] \\ F_s^0 \left(\mathrm{Re}\left[e^{j(\omega+\omega^R)t}\right] + Re\left[e^{j(\omega-\omega^R)t}\right]\right) \end{array} \right\} \qquad (2)$$

$$u(t) = \left\{ \begin{array}{c} X_0 \mathrm{Im}[e^{j(\omega t-\phi_a)}] \\ \displaystyle\sum_{i=1}^{2} Y_{0_i} \mathrm{Re}\left[e^{j[(\omega-(-1)^i\omega^R)t-\phi_a-\phi_{s_i}]}\right] \end{array} \right\} \qquad (3)$$

where t denotes time. In Eqs. (2) and (3) the phase delay, the force amplitude and the displacement amplitudes in each component are defined as follows:

$$\phi_\alpha = \tan^{-1}\frac{\gamma_\alpha}{Q_\alpha(1-\gamma_\alpha^2)} \quad (\alpha = a,\ s_1,\ s_2) \qquad (4)$$

$$F_a^0 = \frac{4\varepsilon h n_c^p}{g_a} V_b V_a \qquad (5)$$

Figures and Tables

Fig. 1　Simplified structure of decoupled microgyroscope
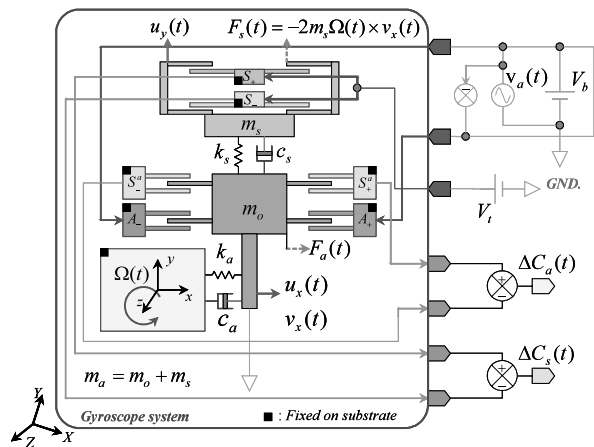

Fig. 2　Mechanical and electrical schematic diagram of decoupled microgyroscope

$$F_s^0 = F_s^0(\omega) = m_s \omega X_0 \Omega_0 \tag{6}$$

$$X_0 = X_0(\omega) = \frac{F_a^0}{k_a} \Theta_a \tag{7}$$

$$Y_{0i} = Y_{0i}(\omega) = \frac{F_s^0}{k_s} \Theta_{s_i} \quad (i = 1, 2). \tag{8}$$

Here, $\gamma_a = \omega/\omega_a$, $\gamma_{s_i} = \dfrac{\omega - (-1)^i \omega^R}{\omega_s}$ $(i = 1, 2)$, $Q_a = \sqrt{m_a k_a}/c_a$, $Q_{s_i} = \sqrt{m_s k_s}/c_s$ $(i = 1, 2)$, and $\omega_\alpha = \sqrt{k_\alpha/m_\alpha}$ $(f_\alpha = \omega_\alpha/2\pi,\ \alpha = a, s)$. In Eq. (5) ε, h, n_c^p and g_a are permittivity, the thickness of the gyroscope structure, the number of total pairs of electrode and gap between the movable and the fixed comb electrodes in y-direction, respectively. In Eqs. (7) and (8) the non-dimensional vacuum magnification factor for each motion are defined as follows:

$$\Theta_\alpha = \frac{1}{\sqrt{(1 - \gamma_\alpha^2)^2 + \left(\dfrac{\gamma_\alpha}{Q_\alpha}\right)^2}} \quad (\alpha = a,\ s_1,\ s_2). \tag{9}$$

For $Q_a \gg 1$, the vacuum magnification factor for driving motion, i.e., Θ_a reaches its maximum value when $\gamma_a = 1$: the driving frequency becomes equal to the driving natural frequency.

2.3 Characteristics of the sensing electrodes

The sensing displacement is expressed in terms of capacitance change. As shown in Figs. 2 and 3, the unit sensing capacitance change ΔC^u is the difference value between top unit capacitance C_+^u and bottom unit capacitance C_-^u, when initial capacitances are the same with each other. The total sensing capacitance change is calculated from multiplying the total number of unit sensing electrodes n_s^q by the unit sensing capacitance.

$$\Delta C_s = \Delta C^u n_s^q = (C_+^u - C_-^u) n_s^q \tag{10}$$

$$C_\pm^u = 2\varepsilon l_{so} h \left(\frac{1}{g_{s1} \mp u_y} + \frac{1}{g_{s2} \pm u_y} \right). \tag{11}$$

In order to convert the capacitance change into the voltage change, a C/V (capacitance/voltage) converter is used, and DC voltage is applied to the C/V converter.
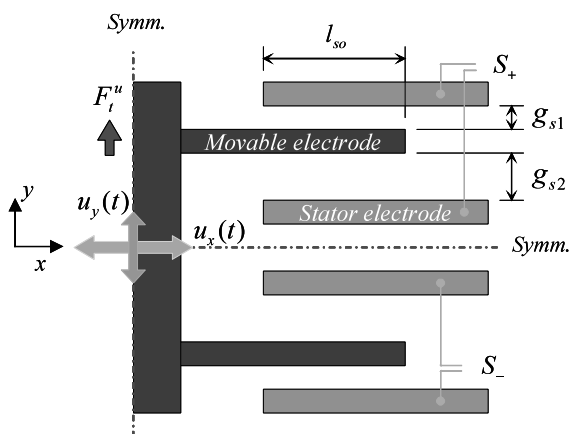

Fig. 3   A unit model of sensing electrodes

The DC voltage V_t has an additional function of tuning voltage that generates tuning force in y-direction and reduces sensing stiffness. The tuning force acting on unit electrodes as shown in Fig. 3 is formulated and its Taylor series expansion leads to the expression for the tuning stiffness and then is expressed as follows:

$$F_T^u = 4\varepsilon l_{so} h V_t^2 \left(\frac{1}{g_{s1}^3} + \frac{1}{g_{s2}^3} \right) \cdot u_y + O\left[\left(\frac{u_y}{g_{s1,2}} \right)^3 \right]. \tag{12}$$

The last term in Eq. (12) is negligible because the ratio of sensing displacement to the gap is considerably less than 1. As a result, the relationship of tuning force and sensing displacement is linear. The electrical tuning stiffness is expressed as follows:

$$k_t^e = 4\varepsilon l_{so} h V_t^2 \left(\frac{1}{g_{s1}^3 + g_{s2}^3} \right) n_s^q. \tag{13}$$

The finial sensing spring constant k_s is obtained by subtracting the electrical tuning stiffness from the mechanical sensing stiffness k_s^m as follows:

$$k_s = k_s^m - k_t^e. \tag{14}$$

The mechanical sensing spring constant with L-shape and the driving spring constant with folded shape are formulated by beam theory (see Appendix A).

2.4 Modeling of the electronic signal processing

At the gyroscope chip level, the sensing output is in the form of the capacitance change and has the two components of frequency around the driving frequency. The final voltage output of the input angular velocity is obtained through the signal processing, which contains C/V conversion process, demodulation and low pass filtering process.

In the process of converting the sensing capacitance change into the sensing voltage change ΔV_s, the C/V converter is used and the sensing voltage change is calculated as follows:

$$\Delta V_s = \alpha_{CV} \Delta C_s \tag{15}$$

where, $\alpha_{CV} = V_t/C_f$ and C_f is the capacitance of the feedback capacitor in the C/V converter.

In order to separate the signal of the input angular velocity from the driving frequency signal, the demodulation should be used: the output signal from C/V converter is multiplied by the driving velocity signal with the unit amplitude. The demodulated signal has a high frequency that is twice of the driving frequency and a low frequency that is the frequency of the input angular velocity. After the demodulated signal passes the low pass filter, the high frequency component is removed and only the low frequency component remains. The final output signal is defined and calculated as follows:

$$[LPF]\{\Delta V_s(t) \cdot \mathrm{Im}[e^{j\omega t}]\} = \Lambda \mathrm{Re}\left[e^{j(\omega^R t - \phi_s)} \right] \tag{16}$$

where Λ is the maximum output amplitude of the gyroscope and ϕ_s is the final phase delay between input and

output signals. The amplitude and phase delay are calculated as follows:

$$\Lambda = \sqrt{\Lambda_1^2 + \Lambda_2^2} \tag{17}$$

$$\Lambda_1 = \frac{\alpha_{CV}}{2} \sum_{i=1}^{2} (-1)^i Y_{0_i} \text{Re}\left[e^{j(\phi_a + \phi_{s_i})}\right] \tag{18}$$

$$\Lambda_2 = \frac{\alpha_{CV}}{2} \sum_{i=1}^{2} Y_{0_i} \text{Im}\left[e^{j(\phi_a + \phi_{s_i})}\right] \tag{19}$$

$$\phi_s = \tan^{-1} \frac{\Lambda_1}{\Lambda_2}. \tag{20}$$

From Eq. (16), the scale factor, or sensitivity, of the gyroscope is defined as follows:

$$S.F.(t) = \frac{\Lambda \text{Re}\left[e^{j(\omega^R t - \phi_s)}\right]}{\Omega(t)}; \quad \Omega(t) = \Omega_0 \text{Re}\left[e^{j\omega^R t}\right] \tag{21}$$

From Eqs. (17)–(21), the scale factor in frequency domain can be expressed as follows:

$$S.F.(\omega) = \frac{\Lambda}{\Omega_0} \tag{22}$$

2.5 Modeling of fabrication tolerance factor

The fabrication processes of the microgyroscope are shown in Fig. 4. In the etching process for the formation of the gyroscope structure, lateral over-etching (*LOE*) and vertical over-etching (*VOE*) exist as shown in Fig. 5 and influence the gyroscope performance parameters. The SOI wafer with the gyroscope structure and the glass wafer with cap structure are anodically bonded in high vacuum to obtain the designed Q factor. The *LOE* and *VOE* are defined as fabrication tolerance factors as shown in Fig. 5 (c). The factors that depend on the location in the gyroscope structure affect all the structural dimensions. The actual dimensions used in analysis of the gyroscope system are defined as follows:

$$W_p = W_p^m - LOE_p \tag{23}$$

$$H_p = H_p^w - VOE_p \tag{24}$$

where the *W*, *H* are in-plane, out-of-plane or height dimensions, respectively and the subscript *p*, superscripts *m*, *w* indicate the location of a structural component, the mask dimension and wafer dimension, respectively. The
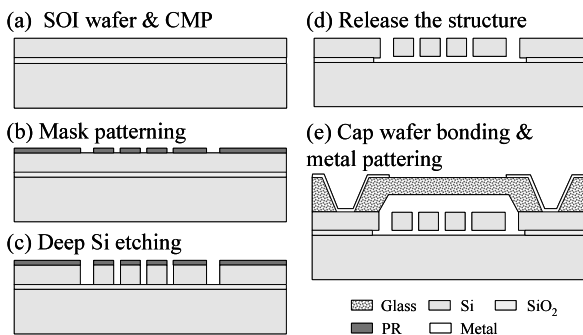
mask and wafer dimensions have the deterministic values as the final design values. The mask dimensions are used in the mask patterning data for structure fabrication and the wafer dimensions in a target thickness data for structure silicon layer in SOI wafer. On the other side the *LOE* and *VOE* have the statistical values which consist of the mean (μ) and standard deviation (σ).

Since the amount of over-etching is almost the same over the regions of one gyroscope chip, we can assume that the variation of the *LOE* and *VOE* occur only between the chips on the wafer. In addition the variation of the height dimension cannot change the frequencies because the change of ratio of the spring constants and the masses due to the variation are the same in this gyroscope system. Therefore, from Eq. (23) the design variables can be expressed as form as follows:

$$W_p = W_p^m - LOE. \tag{25}$$

From now on, we can utilize these actual structural dimensions in the analysis of the gyroscope system and in the MCS, regarding all mask dimensions as deterministic design outputs and taking the *LOE* as the statistical variable applicable to all the structural dimensions. In the case of the analysis which does not required statistical information, only the mean *LOE* is used.

The variation of the Q factor which affects the amplitude of the driving displacement could be another fabrication tolerance factor. However, the amplitude of the driving displacement is kept constant by an automatic gain control (AGC) in ASIC. The damping coefficients are mostly influenced by the geometric topology and the wafer level vacuum package. The effects of the *LOE* on
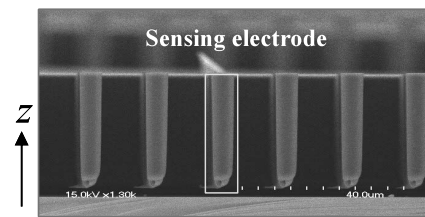
(a)   Fabricated gyroscope structure
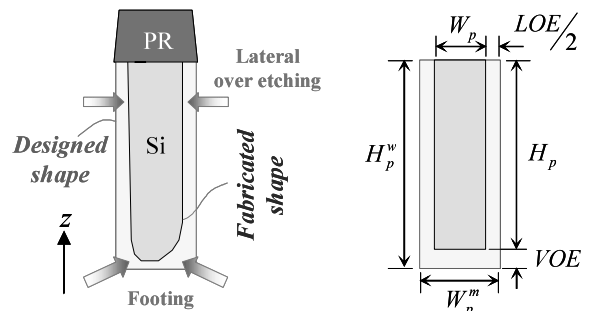
(b)   Fabrication influence   (c)   Design remodeling for fabrication tolerance factor

Fig. 5   Fabrication tolerance factor in gyroscope structure

Fig. 4   Microgyroscope fabrication process

the variation of Q factors are negligible compared with the other main influences, i.e., the geometric topology and the vacuum package. Thus, in the design process, the Q factor was assumed to be independent of the *LOE*.

3. Robust Design of a Decoupled Microgyroscope

A robust optimal design with the multi-objective function of the frequency difference sensitivities is carried out to determine design variables such as spring member dimensions while satisfying the performance specifications of the gyroscope. The fabrication tolerance factor *LOE* was measured and used in the optimal design process.

3.1 Fabrication process capability

The variation in the *LOE* should be determined before the design process. One might attempt to cut the portion of the structure and measure the variation in the *LOE*, but the most of the suspended structures are easily broken. In this study, the mean and the standard deviation of the *LOE* was analytically found without destroying the gyroscope structure. The mean *LOE* was determined as $0.445\,\mu$m by the design compensation for the difference between the analysis result and the fabrication result in the driving natural frequency. The standard deviations of the frequency difference were measured from the fabricated gyroscope chips (Fig. 6). Therefore, the variation in the *LOE* was analytically determined with the condition that the analytical frequency difference should be the same as that measured results. As a result, the standard deviation of the frequency difference was measured as $77.9\,$Hz, the corresponding standard deviation of the *LOE* as $0.337\,\mu$m (Fig. 6). The driving and sensing natural frequencies and their standard deviations were measured as $7\,777.2\,$Hz, $7\,922.55\,$Hz, $84.7\,$Hz, and $111.64\,$Hz, respectively. The designed dimensions and specifications are listed in Tables 1 and 2.

3.2 Performance design

The gyroscope was designed to meet the specifications in the performance parameters such as the scale factor and the phase delay. All the vibratory microgyroscopes are driven at the driving natural frequency to maximize the scale factor. In order to maximize the performance of the gyroscope, the scale factor should be maximized while the phase delay should be minimized. The scale factor and the phase delay are expressed in terms of the frequency difference between the fixed driving frequency and the varying sensing frequency and plotted in Fig. 7. Notice that the scale factor reaches its maximum value when the frequency difference is non-zero. It is partly due to the phase of the multiplier component (in this study, velocity component) in demodulation process. The simulation results of the gyroscope indicated that, as the frequency difference increases, the scale factor and the phase delay decrease. Therefore, the gyroscope was designed within
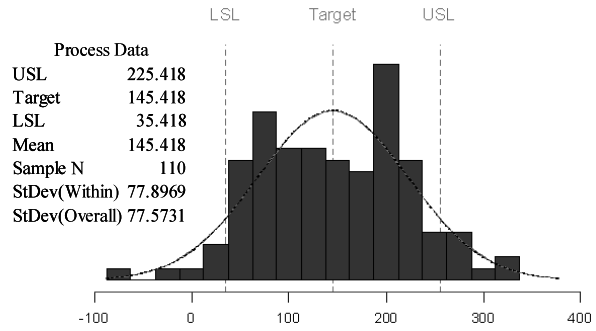
Fig. 6   Process capability analysis for the frequency difference

Table 1   Gyroscope performance data

Voltage V	Q factor	Mass μg	Stiffness μN/μm	Frequency Hz
V_a=0.5 V_b=1.35 V_f=1.5	Q_a=3000 Q_s=300	m_a=67.8 m_s=28.86	k_a=164 k_s=72	f_a^*=7834 Δf^*=88
Input angular velocity		Performance parameters		
Ω_0 = 10 degree/s $f^R = \dfrac{\Omega^R}{2\pi} = 5$ Hz		S.F. = 2.7 mV/deg/s P.D. = 0.95 degree		

Table 2   Initial design variables in mask dimensions (μm)

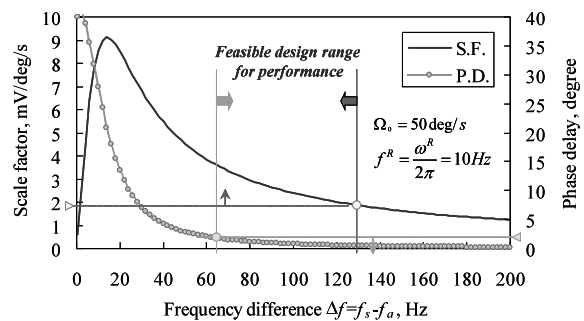| Design variable	Initial	Low limit	Upper limit
x_1^m	5	4	6
x_2^m	4.83	4	6
x_3^m	145	100	174
x_4^m	296	200	690

Fig. 7   Gyroscope performance with respect to frequency difference

the feasible design range in which the specifications of the scale factor and the phase delay were met (Fig. 7).

The dimensions of the driving and sensing spring structures were taken as the design variables (Fig. 8) because the frequencies are sensitive to the spring dimensions that are easily altered in mask drawing process. From Eq. (25) the design variables are denoted as follows:

$$x_i = x_i^m - LOE \qquad (26)$$

where the subscript $i\ (=1-4)$ is the index number of the dimensions. x_i is used in analysis of the gyroscope and

x_i^m in mask dimension as a design result. In this analysis which is not required statistical information, only the mean *LOE* is used. Through the design procedure, the performance data and the design variables are determined as shown in Tables 1 and 2, respectively.

3.3 Robust optimal design

The robust design could be performed in many different ways according to the system characteristics. A gyroscope design can be robust when the difference between the actuating (or driving) frequency and the sensing frequency is insensitive to the variations of design variables. The objective can be generally formulated so as to minimize the maximum sensitivities of the frequency difference with respect to the design variables with uncertainty. In this study, the *LOE* is considered to be constant for all the mask dimensions as shown in Eq. (25). A multi-objective formulation for a robust optimal design of the decoupled gyroscope is proposed as follows:

$$
\begin{aligned}
\text{Find} \quad & x_i^m \quad (i = 1 - 4) \\
\text{To minimize} \quad & \lambda_1 \max\left(\left|\frac{\partial(\Delta f)}{\partial x_i}\right|\right) + \lambda_2 \left|\frac{\partial(\Delta f)}{\partial(LOE)}\right| \\
\text{where} \quad & \Delta f = f_a - f_s \qquad (27) \\
\text{Subjet to} \quad & f_a = f_a^* \\
& \Delta f = \Delta f^* \\
& {}^L x_i^m \leq x_i^m \leq {}^U x_i^m \quad (i = 1 - 4)
\end{aligned}
$$

where λ_1, λ_2 are the weighting factors. The initial design values for the mask dimensions and upper and low limits of these design variables are listed in Table 2. The driving natural frequency and the frequency difference were kept the same as the values used in the initial design. These constraints are needed to keep the performance specification constant during the optimal design process. The target frequency f_a^* and frequency difference Δf^* values are presented in Table 1.

Considering the decoupled gyroscope, the first term in the object in Eq. (27) can be simplified as follows:

$$
\begin{aligned}
\max\left(\left|\frac{\partial(\Delta f)}{\partial x_i}\right|\right) &= \max\left(\left|\frac{\partial f_s}{\partial x_i} - \frac{\partial f_a}{\partial x_i}\right|\right) \quad (i = 1 - 4) \\
&= \max\left(\left|\frac{\partial f_a}{\partial x_1}\right|, \left|\frac{\partial f_s}{\partial x_2}\right|, \left|\frac{\partial f_a}{\partial x_3}\right|, \left|\frac{\partial f_s}{\partial x_4}\right|\right).
\end{aligned}
$$

$$(28)$$
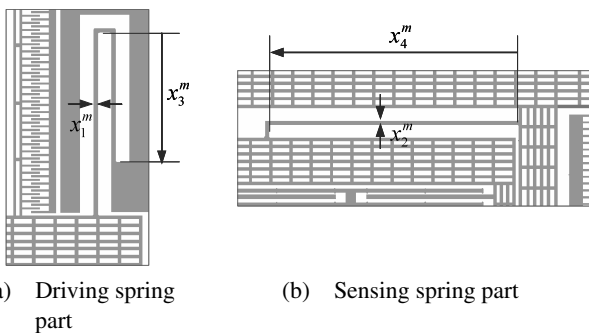

(a) Driving spring part   (b) Sensing spring part

Fig. 8 Design variables for robust optimization

Three cases of the robust optimal design with different weighting factors were investigated. For case I, a conventional robust optimal design was performed by setting $\lambda_1 = 1$, $\lambda_2 = 0$. For case II, a newly presented formulation for the current uncoupled gyroscope with a single fabrication tolerance was studied: $\lambda_1 = 0$, $\lambda_2 = 1$. Last, for the third case, the mixed form of the first and the second was considered, i.e., $\lambda_1 = 1/2\,775$, $\lambda_2 = 1/267$ which were determined as a reciprocal value of each initial sensitivity for normalization.

4. Results and Discussion

Three cases of robust optimal design were performed showing the statistical distributions. We used the MCS and compared the optimal design results with each other.

4.1 Results of robust optimal design

In the optimization, DOT (design optimization tools)[16] is used as a optimization tool with SQP (sequential quadratic programming) as the optimization algorithm. The initial and final optimal design variables are respectively listed in Tables 2 and 3. The distributions of the corresponding frequency difference with respect to the variation of the mean *LOE* are shown in Fig. 9. The frequency difference for the initial case was 267 Hz and it is improved as 180, 24 and 25 Hz, respectively, for cases I, II and III. The improvements of the robustness for the driving frequency with respect to *LOE* are shown in Fig. 10. In cases I and III the change ratios of the sensitivity for the driving frequency about *LOE* were decreased by 9.9 and 8.3%, respectively, but in case II increased by 4.1%.

For case I, which aims to minimize the variation of the frequency itself about *LOE*, the driving and sensing

Table 3   Robust optimization results (μm)

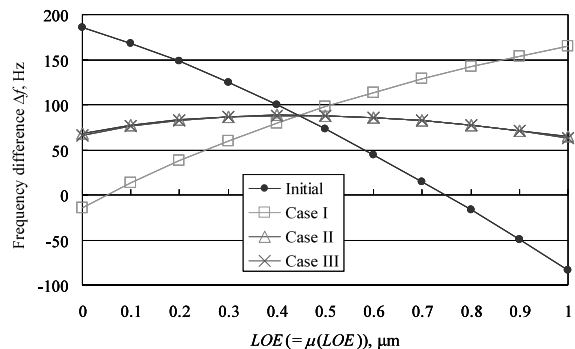| Design variable	Case I	Case II	Case III
x_1^m	5.28	4.89	5.23
x_2^m	6	5.17	5.53
x_3^m	174	131.79	169.59
x_4^m	376.07	319.51	344.06

Fig. 9 Optimization results: frequency difference with respect to *LOE*

spring widths were increased up to the limits satisfying the spring length constraints (Table 3), because the more the spring width is increased, the more the change ratio of the spring width by the same *LOE* is decreased. That is to say, the change ratio of the frequency is also decreased because the frequency is proportional to the cubic of the spring width squared (Fig. 10). For case II, whose purpose is to minimize the variation of the frequency difference about *LOE*, the driving and sensing spring widths were determined when the sensitivities of each frequency with respect to *LOE* are to be the same. The ratio of the sensing spring width to the driving spring width was found as 1.06 (Table 3). For case III, the driving spring width was found to be similar to case I while the spring width ratio similar to case II.

4.2   Certification by Monte Carlos simulation

The Monte Carlos simulation (MCS) was performed to calculate the statistical distribution. First of all, three thousand random samples were generated for the *LOE*, which has the mean of 0.445 μm and the standard devi-

ation of 0.337 μm. In each simulation, the *LOE* was used in all structural dimensions as well as the design variables as expressed in Eqs. (25) and (26). Finally, the optimal values were obtained for each *LOE*, and the distributions of the frequency differences are plotted in Fig. 11.

The improvements of the standard deviations of the frequency difference are listed in Table 4. The standard deviations of the frequency difference are decreased by 24.4%, 79.3%, and 78.2%, respectively, for case I, cases II and III. However, the standard deviations of the driving frequency for cases I and III are decreased by about 10%, while the deviation is increased by 4.1% for case II. In case III, both deviations are decreased.

5.   Conclusion

The initial design of the gyroscope was performed to meet the specifications in the performance parameters of the scale factor and the phase delay. We found that the parameters were dependent upon the frequency difference. The lateral over-etching with the statistical distribution caused by the fabrication process was defined as the fabrication tolerance factor and considered as one component of the design variables. To minimize the influence of
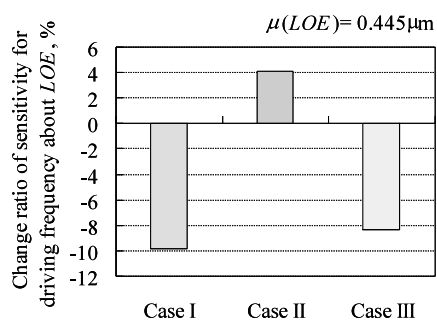

Fig. 10   Improvement of robustness in driving frequency

Table 4   Standard deviation changes from the initial design after robust optimization (%)

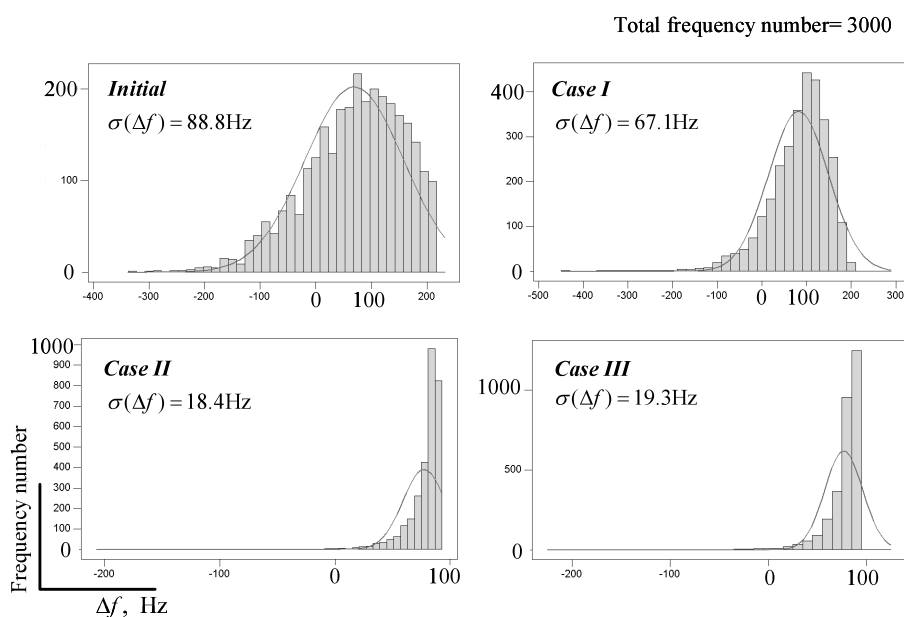| Standard deviation	Case I	Case II	Case III
$\sigma(\Delta f)$	-24.4	-79.3	-78.2
$\sigma(f_a)$	-10.0	4.1	-8.4
$\sigma(f_s)$	-34.4	-11.9	-22.5

Total frequency number= 3000

Fig. 11   Distribution of frequency difference of the three robust optimal design cases: the statistical distribution was simulated using a Monte Carlo method

the fabrication tolerance factor on the decoupled vibratory microgyroscope performance, the robust optimal design was performed. The objective functions were formulated so as to minimize the sensitivities of the frequency difference and frequency itself with respect to the fabrication tolerance factor satisfying the same performance specifications.

It might be possible to adjust the sensing frequency by tuning the DC voltage. However, the tuned DC voltage could change not only the sensing frequency but also the sensing sensitivity. Thus, it is not adequate to adjust the voltage only to tune the frequency.

The robust optimized results were compared with initial design results through the MCS. As a result, the standard deviation of the frequency difference and the driving natural frequency were reduced to 78% and 8%, respectively.

Acknowledgment

Appendix A

The mechanical spring constants of the folded driving and L-shaped sensing springs, as shown in Fig. 12, are analytically derived using a beam theory as follows:

$$k_j^m = EI_j(\Gamma_1^j - \alpha_j \Gamma_2^j - \beta_j \Gamma_3^j)^{-1} \quad (j = a, s) \qquad (A.1)$$

where E denotes Young's modulus, I_j ($= hb_j^3/12$) a mass moment of inertia. The symbols Γ_k^j ($k = 1, 2, 3$), α_j and β_j are defined as follows:

$$\Gamma_1^a = \frac{l_1^3 + l_3^3}{3} + l_1^2(l_2 + l_3) \qquad (A.2)$$

$$\Gamma_2^a = l_1 l_2 l_3 + \frac{(l_1 l_2 - l_3^2)l_2}{2} \qquad (A.3)$$

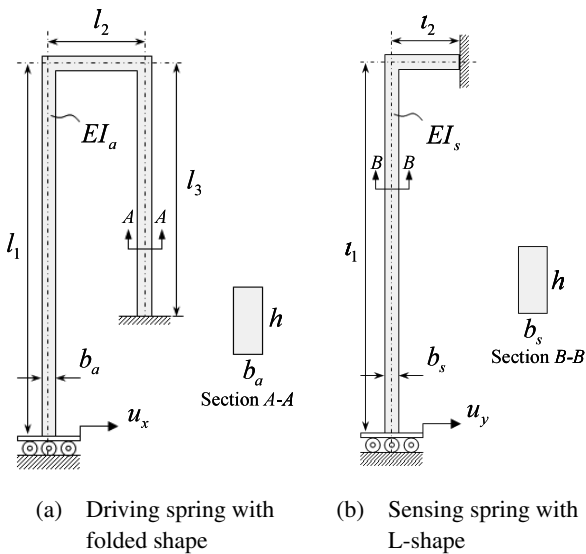(a) Driving spring with folded shape (b) Sensing spring with L-shape

Fig. 12 Geometric configuration and parameter definition of driving and sensing springs

$$\Gamma_3^a = \frac{l_1^2 - l_3^2}{2} + l_1(l_2 + l_3) \qquad (A.4)$$

$$\Gamma_1^s = \frac{\iota_1^3}{3} + \iota_1^2 \iota_2 \qquad (A.5)$$

$$\Gamma_2^s = \frac{\iota_1 \iota_2^2}{2} \qquad (A.6)$$

$$\Gamma_3^s = \frac{\iota_1^2}{2} + \iota_1 \iota_2 \qquad (A.7)$$

$$\begin{Bmatrix} \alpha_j \\ \beta_j \end{Bmatrix} = \mathbf{\Phi}_j^{-1} \begin{Bmatrix} \Gamma_2^j \\ \Gamma_3^j \end{Bmatrix} \qquad (A.8)$$

$$\mathbf{\Phi}_a = \begin{bmatrix} \frac{l_2^3}{3} + l_3 l_2^2 & \frac{l_2^2}{2} + l_2 l_3 \\ Symm. & l_1 + l_2 + l_3 \end{bmatrix} \qquad (A.9)$$

$$\mathbf{\Phi}_s = \begin{bmatrix} \frac{\iota_2^3}{3} & \frac{\iota_2^2}{2} \\ Symm. & \iota_1 + \iota_2 \end{bmatrix}. \qquad (A.10)$$

References

(1) Yazdi, N., Ayazi, F. and Najafi, K., Micromachined Inertial Sensors, Proceedings of the IEEE, Vol.86, No.8 (1998), pp.1640–1659.

(2) Greiff, P., Boxenhorn, B., King, T. and Howe, R.T., Silicon Monolithic Micromechanical Gyroscope, Tech. Dig. 6t Int. Conf. Solid-State Sensors and Actuators Transducers'91, San Francisco, CA, (1991), pp.966–968.

(3) Burdess, J.S., Harris, A.J., Cruickshank, J., Wood, D. and Cooper, G., A Review of Vibratory Gyroscopes, Engineering Science and Education Journal, (1994), pp.249–254.

(4) Oh, Y.S., Lee, B.L., Baek, S.S., Kim, H.S., Kang, S.J. and Song, C.M., A Tunable Vibratory Microgyroscope, Sensors and Actuators A, Vol.64, No.1 (1998), pp.51–56.

(5) Kobayashi, S., Hara, T., Oguchi, T., Asaji, Y., Yaji, K. and Ohwada, K., Double-Frame Silicon Gyroscope Packaged under Low Pressure by Wafer Bonding, The 10th Int. Conf. on Solid-Stage Sensors and Actuators Transducer 99, Sendai, Japan, (1999), 3D1.3.

(6) Adams, S., Grovess, J., Shaw, K., Davis, T., Cararelli, D., Carroll, R., Walsh, J. and Fontanella, M., A Single-Crystal Silicon Gyroscope with Decoupled Drive and Sense, Part of the SPIE Conf. on Micromachined Devices and Components V, Santa Clara, California, Vol.3876 (1999), pp.74–83.

(7) Mochida, Y., Tamura, M. and Ohwada, K., A Micromachined Vibrating Rate Gyroscope with Independent Beams for the Drive and Detection Modes, Twelfth IEEE International Conference MEMS '99, (1999), pp.618–623.

(8) Park, K.Y., Jeong, H.S., An, S., Shin, S.H. and Lee, C.W., Lateral Gyroscope Suspended by Two Gimbals through High Aspect Ratio ICP Etching, The 10th Int. Conf. on Solid-Stage Sensors and Actuators Transducer 99, Sendai, Japan, (1999), 3D2.1.

(9) Baek, S.S., Oh, Y.S., Ha, B.J., An, S.D., An, B.H.,

Song, H. and Song, C.M., A Symmetrical z-Axis Gyroscope with a High Aspect Ratio Using Simple and New Process, Twelfth IEEE International Conference MEMS '99, (1999), pp.612–617.

(10) Tanaka, K., Mochida, Y., Sugimoto, S., Moriya, K., Hasegawa, T., Atsuchi, K. and Ohwada, K., A Micromachined Vibrating Gyroscope, Proceedings of IEEE MEMS '95, (1995), pp.278–281.

(11) Geen, J.A., Sherman, S.J., Chang, J.F. and Lewis, S.R., Single-Chip Surface Micromachined Integrated Gyroscope with 50°/h Allan Deviation, IEEE Journal of Solid-State Circuits, Vol.37, No.12 (2002), pp.1860–1866.

(12) Hwang, K.H., Lee, K.H., Park, G.J., Lee, B.L., Cho, Y.C. and Lee, S.H., Robust Design of a Vibratory Gyroscope with an Unbalanced Inner Torsion Gimbal Using Axiomatic Design, Journal of Micromechanics and Microengineering, Vol.13, No.1 (2002), pp.8–17.

(13) Taguchi, G., Quality Engineering (Taguchi Methods) for the Development of Electronic Circuit Technology, Reliability IEEE Transactions on, Vol.44, No.2 (1995), pp.225–229.

(14) Taguchi, G., Taguchi Methods in LSI Fabrication Process, Statistical Methodology IEEE International Workshop 2001 6th, (2001), pp.1–6.

(15) Han, J.S. and Kwak, B.M., Robust Optimal Design of a Vibratory Microgyroscope Considering Fabrication Errors, Journal of Micromechanics and Microengineering, Vol.11, No.6 (2001), pp.662–671.

(16) DOT, Vanderplaats Research and Development Inc.